Soft Matter

Curvature preference of cubic CsPbBr3 quantum dots embedded onto phospholipid bilayer membranes

Journal:	*Soft Matter*
Manuscript ID	SM-ART-03-2023-000409.R2
Article Type:	Paper
Date Submitted by the Author:	11-May-2023
Complete List of Authors:	Chairil, Ricki; University of Southern California, Mork Family Department of Chemical Engineering and Materials Science Malmstadt, Noah; University of Southern California, Mork Family Department of Chemical Engineering and Materials Science

SCHOLARONE™
Manuscripts

Soft Matter

ARTICLE TYPE

Cite this: DOI: 00.0000/xxxxxxxxxx

Curvature preference of cubic $CsPbBr_3$ quantum dots embedded onto phospholipid bilayer membranes†

Ricki Chairil[a] and Noah Malmstadt[a,b,c]

Received Date
Accepted Date

DOI: 00.0000/xxxxxxxxxx

Curvature-mediated lipid-protein interactions are important determinants of numerous vital cellular reactions and mechanisms. Biomimetic lipid bilayer membranes, such as giant unilammelar vesicles (GUVs), coupled with quantum dot (QD) fluorescent probes, provide an avenue to elucidate the mechanisms and geometry of induced protein aggregation. However, essentially all QDs used in QD-lipid membrane studies encountered in the literature are of the cadmium selenide (CdSe) or CdSe core/ZnS shell type, which are quasispherically shaped. We report here the membrane curvature partitioning of cube-shaped $CsPbBr_3$ QDs embedded within deformed GUV lipid bilayers *versus* that of a conventional small fluorophore (ATTO-488) and quasispherical CdSe core/ZnS shell QDs. In alignment with basic packing theory regarding cubes packed in curved confined spaces, the local relative concentration of $CsPbBr_3$ is highest in areas of lowest relative curvature in the plane of observation; this partitioning behavior is significantly different from that of ATTO-488 ($p = 0.0051$) and CdSe ($p = 1.10{\cdot}10^{-11}$). In addition, when presented with only one principal radius of curvature in the observation plane, no significant difference ($p = 0.172$) was observed in the bilayer distribution of $CsPbBr_3$ *versus* that of ATTO-488, suggesting that both QD and lipid membrane geometry greatly impact the curvature preferences of the QDs. These results highlight a fully-synthetic analog to curvature-induced protein aggregation, and lay a framework for the structural and biophysical analysis of complexes between lipid membranes and the shape of intercalating particles.

1 Introduction

Membrane curvature is a decisive factor in many cell membrane-based molecular interactions. Specifically, membrane proteins are dependent on local curvature to facilitate the production of curved membrane structures[4], and the geometric mismatch between the hydrophobic core of a lipid bilayer membrane and the hydrophobic residues of an integral membrane protein is thought to induce conformational changes in the protein itself[5]. Membrane curvature is also linked to biochemical signaling, with curvature-sensing proteins acting to modulate transmembrane lipid transfer, the tethering of vesicles at the Golgi apparatus, the assembly-disassembly cycle of protein coats, and the generation of lipid rafts[5,6]. Lipid bilayer curvature can also drive protein-protein interactions: curvature-induced protein aggregation (CIPA) has garnered significant attention recently as a mechanism by which the structure of the lipid membrane determines protein functionality and behavior. For instance, capsaicin targets and triggers the pain receptor TRPV1 by reducing the bending modulus of the local lipid bilayer[7], certain enzymes such as cytochrome *c* exhibit maximum activity only when the membrane's mechanical properties are favorable[8], and higher-curvature membranes have been shown to induce higher local concentrations of amyloid-beta peptide(1-40), thus increasing the likelihood of productive nucleation of amyloid fibrils[9]. Embedded protein shape and orientation are believed to be major driving factors behind CIPA; the stability of the resulting domains can be again predicted by considering the thermodynamics of the protein-lipid hydrophobic mismatch, and are consistent with molecular simulations[10,11]. It is clear then that CIPA represents another example of the "second central dogma" of biology[7] – that is, structure dictating function.

Synthetic lipid bilayers, specifically giant unilammelar vesicles (GUVs), are excellent cell membrane models, since they are simple to produce, comparable to cellular size (GUVs commonly range in size from 10-100 μm), and can be fabricated to have a specific and well-controlled lipid composition[12,13]. They are therefore a natural tool in the study of CIPA and its dynamics. Furthermore, quantum dots (QDs), i.e. zero-dimensional semiconducting nanoparticles, have drawn significant attention

[a] *Mork Family Department of Chemical Engineering and Materials Science, University of Southern California, 925 Bloom Walk, HED 216, Los Angeles, CA 90089, USA.*
[b] *Department of Chemistry, University of Southern California, 3620 McClintock Ave., SGM 418, Los Angeles, CA 90089, USA.*
[c] *Alfred E. Mann Department of Biomedical Engineering, University of Southern California, 925 Bloom Walk, HED 216, Los Angeles, CA 90089, USA.*
E-mail: malmstad@usc.edu; Fax: +1 213 740 1056; Tel: +1 213 821 2034
† Electronic Supplementary Information (ESI) available. See DOI: 10.1039/cXsm00000x/

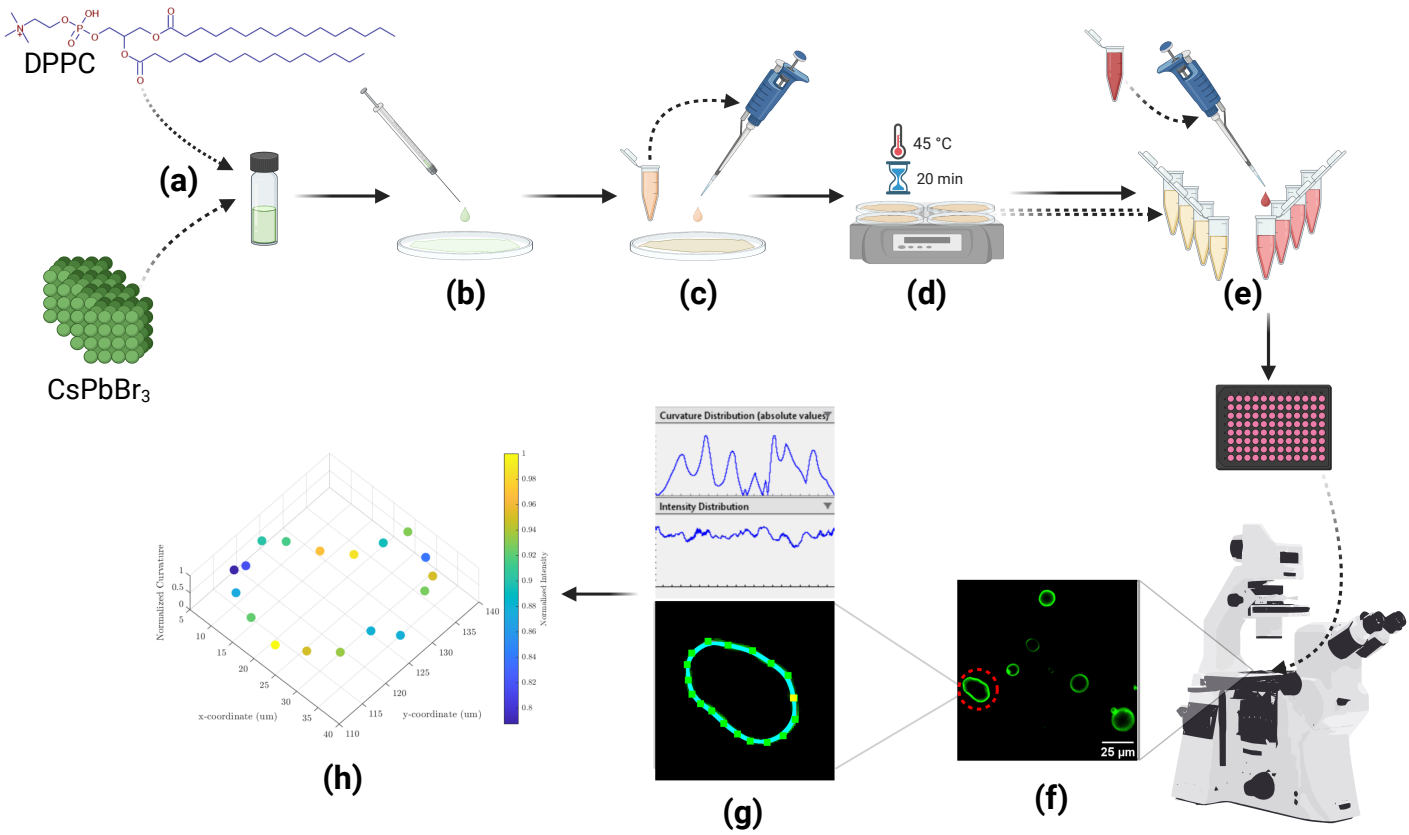

Fig. 1 Overall workflow of curvature preference analysis of fluorescent species embedded in GUV membranes. (a) Dipalmitoylphosphatidylcholine (DPPC) and chosen fluorophore (shown here: $CsPbBr_3$) are combined in chloroform; (b) this solution is deposited in thin layers on an agarose-coated #1 glass coverslip and then (c) swelling solution of 0.1% BSA-200 mM sucrose (orange solution) is added; (d) swelling of lipid leaflets into GUVs proceeds for 20 min on a 45°C hotplate; (e) GUV solutions are transferred to microcentrifuge tubes, osmotically stressed with 212 mM glucose (red solution), allowed to settle, and transferred to 96-well plate or other appropriate observation chamber; (f) GUVs are imaged and qualifying deformed vesicles are chosen to be included in final analysis; (g) the curvature and intensity distributions of candidate GUVs are analyzed in Fiji and Kappa [1,2], *(top)* screenshot of absolute distributions from Kappa, *(bottom)* traced B-spline forming the dataset from Kappa; (h) determine curvature-dependent local concentration of fluorophores *via* MATLAB; example curvature-intensity plot as functions of position is shown. [3]

as superior fluorescent probes for medical imaging of cells and cell components [14,15,16]. For this reason, quantum dots have also been extensively embedded into biomimetic membranes such as GUVs [17,18,19]. However, virtually all state-of-the-art research on quantum dots for cellular imaging involves CdSe or CdSe core/ZnS shell (CdSe/ZnS) QDs, which have a quasi-spherical shape [20]. While these spherical QDs are common due to their ease of synthesis and widespread commercial availability [21], there is a conspicuous lack of study into lipid bilayers embedded with quantum dots other than CdSe or CdSe/ZnS, and, by extension, a gap in understanding how non-spherical particles can be distributed within a cell membrane. In this work, we present a synthetic analog to curvature-driven protein aggregation – namely, a system consisting of cubic $CsPbBr_3$ quantum dots embedded within GUV membranes of variable curvature. By virtue of their rectilinear geometry, we found that that these cubic QDs tend to concentrate in GUV membrane areas with lowest curvature; this is closely similar to how integral membrane proteins selectively aggregate so as to minimize the elastic free energy of bending [8]. In addition, because QDs are far more conformationally restricted than proteins, the system described here can represent a limiting case where aggregation in the lipid membrane is purely driven by "rigid-particle" type interactions (for instance, in the case of amorphous insoluble aggregates of amyloid proteins [9]).

In this work, dipalmitoylphosphatidylcholine (DPPC) GUVs were formed in the presence of cube-shaped $CsPbBr_3$ QDs, quasispherical CdSe/ZnS QDs(hereafter just referred to as CdSe), or a conventional small fluorophore (ATTO-488 conjugated with 1,2-dipalmitoyl-sn-glycero-3-phosphoethanolamine (DPPE), hereafter referred to as just ATTO-488). GUVs are deformed *via* a manipulation of depletion volume effects brought about by encapsulation of biopolymers such as bovine serum albumin (BSA) [22], followed by induced volume reduction by applying an osmotic gradient [23]. This resulted in a drastically skewed volume-to-surface area ratio, causing the GUVs to deform, leading to GUVs with a wide range of curvatures. The curvature and fluorescence intensity of the vesicles were then analyzed to determine what curvature environment a given fluorescent species tended to localize. The entire process is summarized in Fig. 1.

2 Materials and Methods

2.1 Materials

1,2-dipalmitoyl-sn-glycero-3-phosphocholine (DPPC), was obtained from Avanti Polar Lipids (Alabaster, AL, USA). ATTO-488 conjugated with 1,2-dipalmitoyl-sn-glycero-3-phosphoethanolamine (DPPE) was obtained from Sigma-Aldrich (St. Louis, MO, USA) and manufactured by ATTO-TEC GmbH (Siegen, Germany). Cs_2CO_3, PbO, and oleic acid were obtained from Sigma-Aldrich (St. Louis, MO, USA). Tetraoctylammonium bromide (TOAB) was purchased from Beantown Chemical (Hudson, NH, USA). Ultra-low gelling temperature agarose, bovine serum albumin (BSA), glucose, and sucrose were obtained from Sigma-Aldrich (St. Louis, MO, USA). All other general chemicals and solvents (e.g. chloroform and hexanes) were used as provided by Sigma-Aldrich (St. Louis, MO) or Thermo-Fisher Scientific (Waltham, MA, USA).

2.2 Quantum Dots

Fluorescent quantum dots (QDs) were used extensively in this work. Cadmium selenide QDs with emission wavelength peak at 520 nm (CdSe-520 or CdSe) were purchased from Ocean NanoTech, LLC (San Diego, CA, USA); these QDs have a typical ZnS shell and are stablized by olelylamine ligands. CdSe-520 was supplied in solutions of 10 mg mL^{-1} in toluene and have a TEM-verified size of 6 nm from the vendor.

Cesium lead bromide ($CsPbBr_3$) was produced as described in our previous work[24]; briefly, a 10 mM Cs^+/Pb^{2+} precursor solution was prepared in 317 mM oleic acid and hexanes (instead of toluene), alongside a 40 mM Br^- precursor solution also prepared in 317 mM oleic acid and hexanes. To produce the $CsPbBr_3$ QDs, the two precursor solutions were mixed in a 1:1 volume ratio; yellowish-green $CsPbBr_3$ nanocrystals form within seconds. The cubic morphology of our $CsPbBr_3$ nanoparticles was verified *via* TEM in our previous work[24] and have a typical size of 5-8 nm.

2.3 GUV Preparation and Observation

Deformed GUVs were prepared according to a modified agarose-mediated swelling method described in our previous work[25]. Briefly, DPPC at 2 mg/mL was combined with the appropriate fluorescent species (250 μM of $CsPbBr_3$, 250 μM of CdSe-520, or 30 μg ml^{-1} ATTO-488) in chloroform. Based on desired yield, 10 to 15 μL of these solutions were deposited in thin layers on a glass coverslip coated with ultra-low gelling temperature agarose, the solvent evaporated by gentle air stream, and then swelled with 450 μL of an aqueous solution of 0.1% BSA-200 mM sucrose. These coverslips, mounted on Sykes-Moore chambers[26], were then placed on a heating block at 45°C for 20 minutes.

Afterwards, 400 μL of the harvested GUV solution was added to 700 μL of a hypertonic settling solution of 333 mM glucose in a 1.7 mL microcentrifuge tube, for a final glucose concentration of 212 mM. The GUVs were allowed to settle for 20-30 min, after which 200 μL of the settled solution from the bottom of the tube was transferred to 96-well microplates. Observation of the GUVs was performed at ambient room temperature using a Zeiss Axio Observer Z1 optical widefield microscope outfitted with a Colibri 2 light source, which provides illumination at 365, 470, 555, or 625 nm. All three fluorescent species ($CsPbBr_3$, CdSe-520, and ATTO-488) were excited at 470 nm, and the emission wavelengths were set to 520 nm in all cases. Typically, an illumination intensity of approximately 30 mW at 20x magnification (9.5 mW at 40x magnification) and 470 nm, with an exposure time of 200 ms, was used for all imaging; these conditions were kept constant for all images[13].

2.4 Curvature Analysis and Statistics

GUVs were selected for inclusion into the curvature analysis according to the following criteria, which were applied uniformly across all samples:

- They must be isolated from other vesicles or debris; apparent budding from the parent vesicle was judged as a normal consequence of deformation and was considered permissible[23],
- Apparent multilammelar structures were omitted,
- Their shapes must be appropriately deformed, i.e. immediately and obviously non-spheroidial,
- Intensity signals must be sufficiently high to distinguish against background; a difference of >30 corrected intensity units out of a maximum 16-bit intensity value of 65535, or a signal-to-noise ratio of at least 1.6, whichever was greater, was judged sufficient, per the line intensity profile test employed previously[25],
- Vesicle cross-sections must be approximately flat so that the entire vesicle membrane appears in focus.
- Vesicle interiors must be clean and free of debris.

Any puncta or small detritus in the lumina of GUVs were also excluded. It was assumed that the intensity (normalized to the maximum for a particular vesicle; see Results section) corresponds directly to the relative concentration of fluorescent species along the GUV membrane.

Image processing was performed in Fiji[2]. Membranes were manually traced using Kappa, a built-in Fiji curvature analyzer plugin which employs B-splines from a user-generated curve[1]. Details on this curvature calculation, as well as safeguards against sampling biases, are given in the ESI. The curvature analysis was performed in averaging mode to avoid oversampling. The relative curvature and intensity were calculated at every sampled location along the membrane for each selected GUV (details in the Results section). Finally, once the curvature-intensity distributions for all vesicles of a treatment were obtained, they were visualized and analyzed in MATLAB.

3 Results and Discussion

3.1 Generating regions of different curvature *via* lipid bilayer deformation

Ordinary spherical giant unilammelar vesicles (GUV) are defined by only one radius of curvature R_c in the xy-plane. Therefore, they

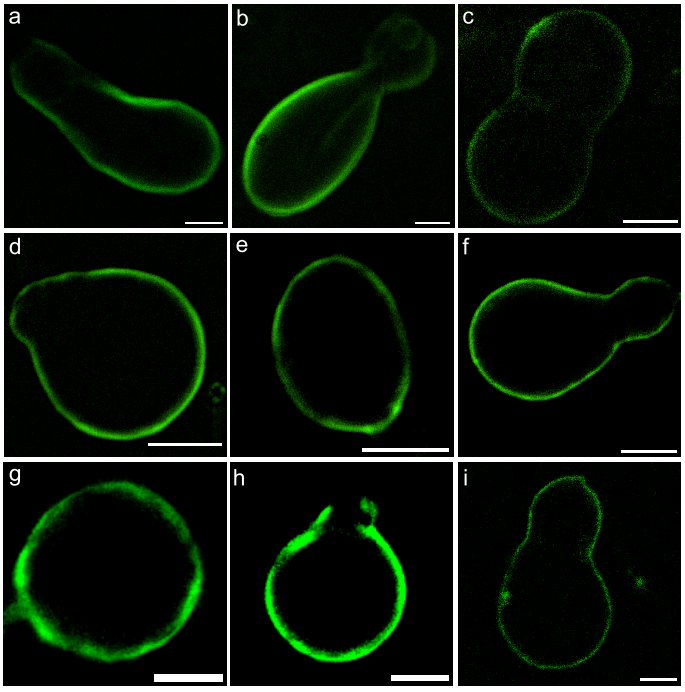

Fig. 2 Representative images of GUVs embedded with (a)-(c) $CsPbBr_3$, (d)-(f) ATTO-488, (g)-(i) CdSe. Scale bars are 10 μm

are ill-suited for studying potential curvature partitioning behavior of various fluorescent species employing familiar microscopy methods. Here, GUVs were deliberately deformed *via* osmotic stress and biopolymer encapsulation to generate non-spherical shapes with multiple distinct curvature regions. This approach is consistent with the area-difference-elasticity (ADE) model of vesicle shape prediction[27,22]; briefly, (i) polymeric molecules inside vesicle lumina tend to aggregate in such a way to minimize the immediate volume around them (the depletion volume V_d), potentially changing the shape of the vesicle's entire enclosed volume if the magnitude of this thermodynamic driving force is sufficiently great, and (ii) the application of a hypertonic ($c_{outside} > c_{inside}$) osmotic sugar gradient reduces the enclosed volume-to-membrane area ratio, further coaxing deformation *via* effluent water flux[23]. From a thermodynamic perspective, only one of these techniques is required to achieve the desired deformation, though in practice, implementing both (i) and (ii) will maximize the yield of deformed GUVs.

To generate deformed GUVs, we employed a modified version of the hydrogel-mediated swelling method[25] whereby the sucrose swelling solution was doped with BSA. Heating at 45°C was necessary to bring the DPPC above its phase transition temperature (T_g = 41°C)[19]. Observations made above the transition temperature are described in the ESI (Sections S2-S4). Because temperature represents a potential confounding factor, increasing nanoparticle mobility in liquid phase vs. gel phase membranes, this work focuses on observations taken at room temperature, i.e. below the gel transition temperature of DPPC. It is expected that there is little to no conformational change in the lipid tails in the gel phase][28,29]; thus, the conformational change of the lipid tails required to accommodate the new QDs most likely happens during the fluidization of the lipid membrane during the heating and swelling step described previously.

After the vesicles were osmotically shocked by placing into glucose settling solution ($(c_{glucose} - c_{sucrose})$ = 12 mM or about 0.3 atm osmotic pressure difference), we observed sizeable populations of deformed vesicles consistent with these hypertonic conditions[23] – oblate, dumbbell, and pear shapes, naturally characterized by relatively high ratios of low-to-high curvature zones, were most common. By our estimation, 50-70% of the vesicles observed were deformed, with the balance remaining spherical or quasi-spherical.

Deformed vesicles fitting the selection criteria were imaged and analyzed to produce curvature-intensity distributions for each of the three fluorescent species. Specifically, every image was first corrected appropriately for dark current and background noise via ImageJ's built-in background subtraction algorithm[30]. Three representative vesicle images for each of the three different conditions are shown in Fig. 2 (a)-(i). To determine local curvature at points along the GUV perimeter, the deformed membranes were traced in Kappa in closed B-spline mode, generating a value for curvature at each point along the spline[1]. Pixel intensity values were also measured at each point along the spline. In this process, oversampling the membranes, i.e. counting the same location more than once beyond the resolution of the images taken, must be avoided. Based on an image resolution of 0.16 μm/pixel, a typical 20-40 μm GUV membrane perimeter is comprised of approximately 400-800 pixels. It was observed that Kappa's individual (non-averaged) sampling mode generates hundreds of locations along a typical membrane, which was exceedingly close to this oversampling limit – prompting use of its auto-averaging sampling algorithm (approx. 15-30 sampling locations per vesicle) instead.

Normalization of the curvatures and intensities for all vesicles was based on the maximum curvatures and intensities observed at each individual vesicle j, at each of the i number of average locations along the membranes, as auto-generated by Kappa:

$$\bar{\kappa}_{i,j} = \left| \frac{\kappa_{i,j}}{\kappa_{max,j}} \right| \quad (1)$$

$$\bar{I}_{i,j} = \frac{I_{i,j}}{I_{max,j}} \quad (2)$$

where

- $\bar{\kappa}_{i,j}$ = the normalized curvature at location i for vesicle j
- $\kappa_{i,j}$ = the actual curvature value at location i for vesicle j [=] μm^{-1}
- $\kappa_{max,j}$ = the maximum curvature value for vesicle j [=] μm^{-1}
- $\bar{I}_{i,j}$ = the normalized intensity at location i for vesicle j
- $I_{i,j}$ = the actual intensity value at location i for vesicle j
- $I_{max,j}$ = the maximum intensity value for vesicle j

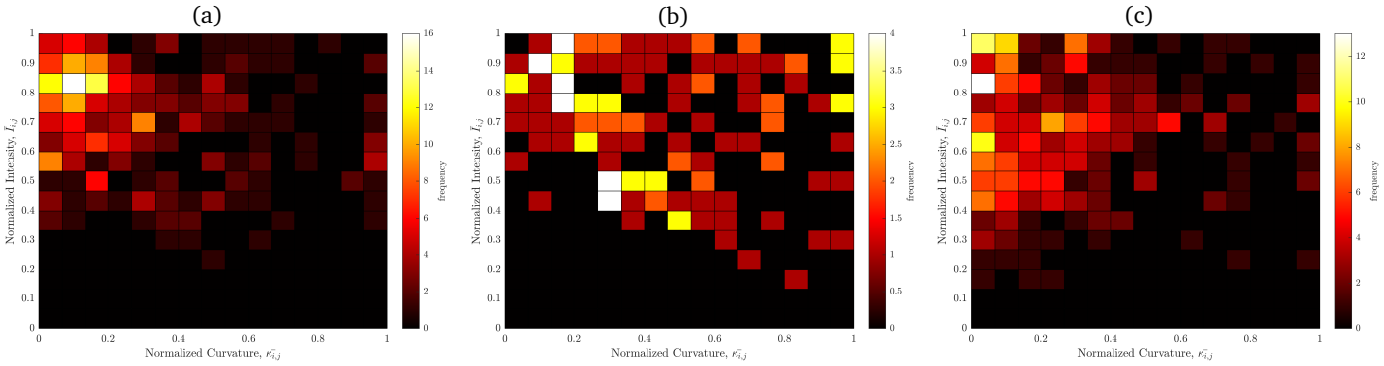

Fig. 3 Histograms depicting the intensity distributions for deformed DPPC membranes embedded with (a) $CsPbBr_3$, (b) CdSe, and (c) ATTO-488.

This normalization provides a convenient scaling whereby the degree of fluorescence partitioning along every membrane location, i, can simply be described using an ordered pair with coordinates $(\bar{\kappa}_{i,j},\bar{I}_{i,j})$ constrained by the unit square with vertices (0,0)(0,1)(1,0)(1,1). The total number of unique pairs $(\bar{\kappa}_{i,j},\bar{I}_{i,j})$ analyzed was $n_1 = 314$ across 10 $CsPbBr_3$-treated and deformed GUVs, $n_2 = 142$ across 9 CdSe-520-treated GUVs, and $n_3 = 330$ across 10 ATTO-488-treated GUVs. GUVs were produced over 3-4 different days across several months and under the same experimental conditions. Thus, potential differences in formulation, batch-to-batch variability, and other time-dependent effects are all represented in these data.

3.2 Curvature preferences of $CsPbBr_3$ quantum dots

Bivariate histograms of each of the curvature-intensity distributions were created using the MATLAB `hist3` function[31]. To minimize the risk of obscuring important trends, the Rice rule (an improvement of the common Sturges' rule) for bin width was employed to divide the domain of the data into fifteen equal bins ($2(300)^{1/3} \sim 15$) along the horizontal $\bar{\kappa}_{i,j}$ and vertical $\bar{I}_{i,j}$ axes[32]. These visualizations are shown in Fig. 3 and provide evidence that the cubic $CsPbBr_3$ QDs studied tend to cluster most prominently in membrane zones having the lowest normalized curvature for their respective vesicles. This is consistent with basic packing theory – cube-shaped particles constrained within a curved envelope will tend to pack more densely along areas where curvature is lowest; indeed, the surfaces defined by a well-ordered arrangement of closely-packed cubes have zero or near-zero curvature[33,34]. Conversely, it can be shown that the number density of maximally-packed, non-interacting circles into a rectangular enclosure of fixed area[35] is lower than that of equal-area squares by roughly 10-18% or more, depending on the area of circle/square chosen. The preference for low-$\bar{\kappa}_{i,j}$ regions is also apparent in the representative vesicles shown in Figs. 2(a)-(c) – note how the green fluorescence tends to be brightest where the radius of curvature R_c is highest for those vesicles ($\bar{\kappa}_{i,j} \sim 1/R_c$), and dimmest at the very highly-curved poles.

3.3 Curvature preferences of CdSe-ZnS core-shell quantum dots

The curvature-intensity distribution of spherical CdSe-520 QDs is shown in Fig. 3(b). Fifteen bins per axis were used despite the smaller sample size to maintain visual consistency. In contrast to the clear preference for lower-curvature regions of $CsPbBr_3$, CdSe was distributed more sporadically throughout the DPPC vesicle membranes. There were two main "modes" of CdSe partitioning observed - (i) a quasi-uniform distribution of CdSe around the membrane as seen in Fig. 2(g)-(i) and (ii) clusters of QDs. Approximately 30% of the CdSe-treated GUVs matching the GUV selection criteria prominently displayed this accumulation phenomenon, and were omitted from the final analysis.

There are several potential reasons for this varied aggregation behavior. For one, it has been widely reported that quantum dot-lipid systems will adopt one of two morphologies depending on the characteristic nanoparticle size D_{QD} and the membrane elastic interface energy change ΔE_{def} associated with membrane "wrapping" about the particles - a quantum dot-micelle complex (QMC) or a quantum dot-liposome complex (QLC)[36,18,37]. QLCs consist of nanoparticles embedded fully within a lipid bilayer, whereas QMCs are the reverse configuration - lipid bilayers fully covering an interior of single (or multiple) QDs. When the QD size distribution straddles a certain critical size D_{crit}, corresponding to the point where ΔE_{def} is equal for both QLC and QMC states, one would expect to observe both QLC and QMC structures[18,37]. QMC structures in particular are manifested in optical microscopy by small, bright lipid-QD aggregates[18]. The critical D_{crit} for the 18-acyl-carbon unsaturated lipid 1,2-dioleoyl-sn-glycero-3-phosphocholine (DOPC) was previously reported as approximately 6.5 nm[18]; if we assume DPPC (16 acyl-carbon) has a similar D_{crit}, then it might be reasonable to expect the formation of some CdSe QMCs and some QLCs, since our CdSe-520 has a TEM-verified size of approximately 6 nm including ligands. Another possibility for the scattered membrane distribution of CdSe is the formation of micropores due to CdSe adhesion[13]. This poration also tends to cause accumulation of both membrane and nanoparticle aggregates at points of attachment, and was reported to be most pronounced with cationic particles[13]. Examples of this extraneous aggregation behavior for the CdSe treatment can be seen in the ESI.

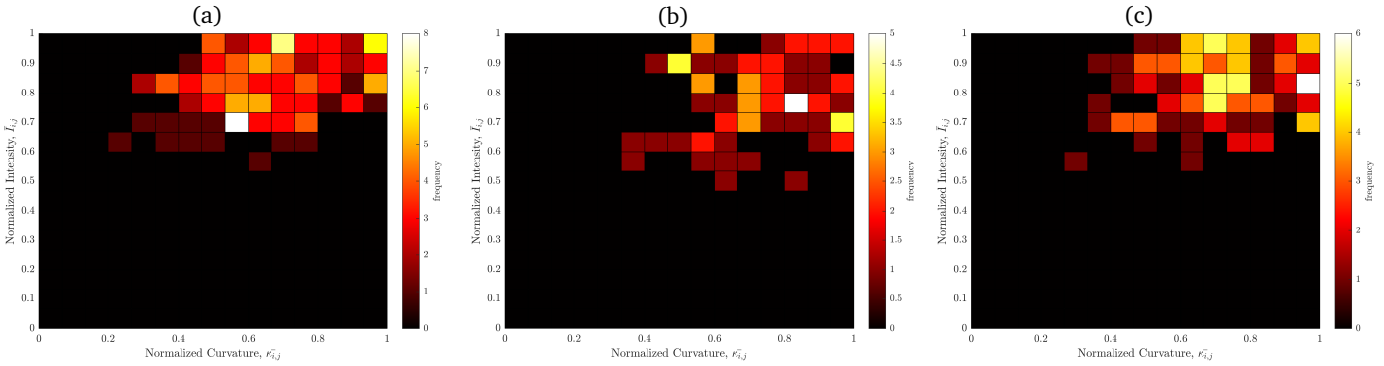

Fig. 4 Histograms depicting the intensity distributions for non-deformed DPPC membranes embedded with (a) $CsPbBr_3$, (b) CdSe, and (c) ATTO-488.

3.4 Curvature preferences of ATTO-488

The curvature-intensity distribution of the control fluorophore, ATTO-488, is depicted in Fig.3(c). While there is a population of ATTO-488 in membrane areas of lower curvature, this is likely due to the high proportion of deformed vesicles naturally possessing more low-curvature membrane regions than high-curvature. Vesicle shapes that are very highly curved throughout, such as clovers or starfish, were rarely seen under the chosen experimental conditions. Nonetheless, ATTO-488 is far more likely to take on a wider range of intensity values than $CsPbBr_3$, demonstrating that we have controlled for potential shape effects. In other words, the local relative concentration of ATTO-488 in low-curvature areas can be high or low, whereas that of $CsPbBr_3$ is almost exclusively high. A quantitative analysis of the centroids of all curvature-intensity distributions, as well as the average Euclidian distance to these centroids, can be found in Table 1; these results show that, despite a tendency towards vesicle shapes with gentler overall curvatures, $CsPbBr_3$ still has about a 10% higher mean normalized intensity in these lower curvature regions than does ATTO-488.

3.5 Curvature preferences of fluorescent species in the limit of spherical and quasi-spherical GUVs

To highlight additionally the curvature-dependent effect of cubic $CsPbBr_3$, control experiments were set up whereby the GUVs were left undeformed. To do this, the same agarose swelling protocol described in Section 2.3 was performed, except that BSA was omitted from the swelling solution formulation, and the external glucose concentration was maintained at 200 mM (instead of 212 mM) to match the interior sucrose concentration. This before-after comparison of undeformed vs. deformed GUVs follows the same methodology and control conditions as those of past works[22,23] studying the osmotic deformation of GUVs. The curvature-intensity analysis described above, using Equations 1 and 2, Kappa, and MATLAB, was performed, this time on spherical and quasi-spherical GUVs. In total, the number of $(\bar{\kappa}_{i,j},\bar{I}_{i,j})$ pairs was $n_1 = 148$ across 11 $CsPbBr_3$-treated un-deformed GUVs, $n_2 = 77$ across 6 CdSe-520-treated GUVs, and $n_3 = 117$ across 10 ATTO-488-treated GUVs. The curvature-intensity distributions for these control vesicles are shown in Fig. 4 (a)-(c).

Because spherical and quasi-spherical vesicles have a much narrower range in curvature values than those associated with deformed vesicles (see Fig.3), by definition of the normalized curvature per Eq. 1 one would expect that a majority of the observed points will be clustered near $\bar{\kappa}_{i,j} = 1$. Similarly, by Eq. 2, if the local concentration of fluorescent species is essentially invariant regardless of position along the lipid bilayer, one would expect that $\bar{I}_{i,j} \approx 1$ for a majority of the points across all $\bar{\kappa}_{i,j}$. Both of these behaviors were observed for all three fluorescent species, as in Fig. 4 (a)-(c). Small excursions from the extreme top-right corner exist due to Kappa's high sensitivity to small changes in manually-drawn B-splines[1], but the overall trend is apparent – all three fluorescent species are partitioned relatively uniformly throughout the lipid bilayer in the limit of minimally-deformed, spherical vesicles. This is in stark contrast to the deformed vesicle partitioning behavior seen in Fig. 3(a)-(c), suggesting that cubic $CsPbBr_3$ has a strong preference towards areas of $\bar{\kappa}_{i,j}$ approaching 0, if they exist in the vesicle on which it resides.

To summarize, the centroids and average distances to these centroids of all bivariate histograms (Fig. 3(a)-(c) for deformed, and Fig. 4(a)-(c) for non-deformed) can be found in Table 1.

Table 1 Normalized curvature and intensity "means" (approximated by data centroids) and average Euclidian distance to these means, of fluorescent-tagged GUVs before and after deformation.

	Deformed		
	$CsPbBr_3$	ATTO-488	CdSe
centroid value, $\bar{\kappa}_{i,j}$	0.27	0.26	0.49
centroid value, $\bar{I}_{i,j}$	0.72	0.67	0.70
mean Euclidian distance to centroid	0.26	0.27	0.31
	Non-deformed		
	$CsPbBr_3$	ATTO-488	CdSe
centroid value, $\bar{\kappa}_{i,j}$	0.67	0.72	0.67
centroid value, $\bar{I}_{i,j}$	0.83	0.83	0.80
mean Euclidian distance to centroid	0.18	0.18	0.22

3.6 Comparison of curvature-intensity distributions

A more rigorous comparison of these distributions is necessary to determine whether or not the observed differences are statistically significant. The null hypothesis H_0 tested is as follows: given two different GUV fluorescent treatments (1) and (2), the

fluorescent species partition themselves in statistically the same way, regardless of membrane curvature. The two-sided, two-dimensional, non-parametric Kolmogorov-Smirnov test proposed by Peacock[38] offers a convenient means of analysis which resolves the problem of multi-directionality of the cumulative distribution function in 2D *via* validation using Monte-Carlo simulations. A MATLAB function based on Peacock's work[39] was employed on the unbinned distribution data to compare every pair of curvature-intensity distribution in this work. Estimated p-values for both deformed and undeformed vesicles are shown in Table 2.

Table 2 Two-dimensional Kolmogorov-Smirnov test statistics D_n and estimated p-values[38,39] on fluorescent-tagged GUVs before and after deformation.

Comparison	deformed GUVs?	D_n	p-value
$CsPbBr_3$ *vs.* ATTO-488	No	0.197	0.172
$CsPbBr_3$ *vs.* CdSe	No	0.289	0.0127
CdSe *vs.* ATTO-488	No	0.213	0.299
$CsPbBr_3$ *vs.* ATTO-488	Yes	0.175	0.0051
$CsPbBr_3$ *vs.* CdSe	Yes	0.372	$1.10\cdot 10^{-11}$
CdSe *vs.* ATTO-488	Yes	0.371	$7.10\cdot 10^{-12}$

Table 1 indicates that $CsPbBr_3$ distributes along the lipid bilayers differently than does ATTO-488 or CdSe ($p \ll 0.05$), corroborating the differences apparent in the histograms in Fig. 3(a)-(c). Crucially, $CsPbBr_3$ and ATTO-488 partition identically ($p > 0.05$) along the lipid membrane per Figs. 4(a) and (c), if no large membrane curvature differences are induced via deformation. CdSe and ATTO-488 are also predicted to partition identically ($p > 0.05$) in this control condition. It is also noted that CdSe partitioning behavior is different ($p < 0.05$) from $CsPbBr_3$ in all cases, at least partly due to the tendency of this material to distribute somewhat differently than the cubic QDs (even in the included datapoints), as discussed in Section 3.3.

3.7 Connecting particle geometry to membrane bending energy

A simplistic analysis of particle geometry and membrane bending energy is consistent with the observations described here. Consider a patch of deformed lipid bilayer membrane with surface area A and lipid intrinsic curvature magnitude κ_0. The contribution of Gaussian curvature can be neglected, since no statistically significant difference in the fluorescence distributions between points of negative curvature and those of positive curvature were observed for the $CsPbBr_3$ treatment - see ESI for more details. The elastic free energy of bending, ΔG_B of this membrane segment, then, is[8]:

$$\Delta G_B = \frac{k_c A(\kappa_1 + \kappa_2 - \kappa_0)^2}{2} \tag{3}$$

where κ_1 and κ_2 are the first and second principal curvatures respectively of the membrane, and k_c is the membrane bending modulus. We will assume that one principal curvature of all points in the GUV membrane is the curvature of the GUV equatorial plane and the other principal curvature is on the order of the inverse of the GUV radius, which generally depends on the points chosen; however, here we will approximate them as the same value $\kappa_1 = \kappa_2 = \kappa_{i,j}$. If this membrane patch is packed with N particles, each of area A_p, then the area packing fraction is $\eta = NA_p/A$[40]. Hence rewriting Eq. 3 in terms of the packing fraction η:

$$\Delta G_B = \frac{k_c N A_p (2\kappa_{i,j} - \kappa_0)^2}{2\eta} \tag{4}$$

A visualization of the terms in this expression for different packing geometries can be found in the ESI.

The membrane's conformational energy associated with lipid hydrocarbon tail deformation depends on the embedded particle size[36]. Because the $CsPbBr_3$ and CdSe quantum dots are of similar size, this energy would be roughly the same in these cases. Hence, the contribution of lipid conformational energy was neglected in this analysis.

Applying Eq. 4 to packing of an equal number N of cubic (C) and spherical (S) particles of the same characteristic side length or diameter s, the ratio of bending energies can be written as

$$\frac{\Delta G_{B,C}}{\Delta G_{B,S}} = \frac{6}{\pi}\frac{\eta_S}{\eta_C}\frac{(2\kappa_{i,j,C} - \kappa_0)^2}{(2\kappa_{i,j,S} - \kappa_0)^2} \tag{5}$$

where

- $\Delta G_{B,C}$ = the bending free energy of the cube particle-packed configuration
- $\Delta G_{B,S}$ = the bending free energy of the sphere particle-packed configuration
- $\kappa_{i,j,C}$ = the absolute curvature of the membrane for the cube particle-packed configuration
- $\kappa_{i,j,S}$ = the absolute curvature of the membrane for the spherical particle-packed configuration
- η_C = the packing fraction of cubic particles in the membrane
- η_S = the the packing fraction of spherical particles

Because it was observed that the direction of curvature was unimportant for the embedded particles' curvature preferences, $\kappa_{i,j,C}$, $\kappa_{i,j,S}$, and κ_0 are taken as absolute values (>0) only.

While Eq. 5 has many degrees of freedom and potential interdependencies, for the sake of simple comparison, consider the case where both membrane packing configurations are equally thermodynamically favored, i.e. $\Delta G_{B,C}/\Delta G_{B,S} = 1$, and where both particle shape configurations have identical packing fractions, i.e. $\eta_S/\eta_C = 1$. In this scenario, it must hold that

$$\frac{(2\kappa_{i,j,C} - \kappa_0)}{(2\kappa_{i,j,S} - \kappa_0)} \sim \sqrt{\frac{\pi}{6}} \tag{6}$$

That is, in order for cubes of side length s and spheres of diameter s to have identical degrees of packing in separate membranes with equal thermodynamic preference for formation (on a purely bending-energy basis), the local curvature of the membrane in the cubic particle-packed case must be lower than that in the spherical particle-packed case.

Next, consider the case of two different-curvature membrane patches (1,2), with lower curvature in location 1 than in location

2 ($\kappa_{C,1} < \kappa_{C,2}$). Both membranes are packed with cubes of equivalent side length. Considering only the free energy of bending ratio,

$$\frac{\Delta G_{B,1}}{\Delta G_{B,2}} = \frac{\eta_2}{\eta_1} \frac{(2\kappa_{C,1} - \kappa_0)^2}{(2\kappa_{C,2} - \kappa_0)^2} \tag{7}$$

The subscripts 1 and 2 represent the corresponding membrane patch. From this estimate, in the case of equal thermodynamic favorability ($\Delta G_{B,1}/\Delta G_{B,2} = 1$), one can arrive at

$$+\sqrt{\frac{\eta_1}{\eta_2}} = \frac{2\kappa_{C,1} - \kappa_0}{2\kappa_{C,2} - \kappa_0} \tag{8}$$

Therefore, because $\kappa_{C,1} < \kappa_{C,2}$, it can be reasoned that the packing of cubes in membrane location 1 is higher than in location 2.

Finally, if the equal-packing condition is relaxed, then

$$\frac{\eta_S}{\eta_C} = \frac{\pi}{6} \frac{(2\kappa_{i,j,S} - \kappa_0)^2}{(2\kappa_{i,j,C} - \kappa_0)^2} \tag{9}$$

and it follows that in the high curvature case, i.e. if

$$\kappa_{i,j,S} > \frac{1}{2}\left(\sqrt{\frac{6}{\pi}}\left(2\kappa_{i,j,C} - \kappa_0\right) + \kappa_0\right) \tag{10}$$

then $\eta_S/\eta_C > 1$; similarly in certain low curvature cases, if

$$\kappa_{i,j,C} < \frac{1}{2}\left(\sqrt{\frac{\pi}{6}}\left(\kappa_0 - 2\kappa_{i,j,S}\right) + \kappa_0\right) \tag{11}$$

then $\eta_S/\eta_C < 1$ (the other root is discarded since it predicts higher cube packing at higher curvatures, contrary to packing theory[35]). Also note that setting $\kappa_{i,j,C} = \kappa_{i,j,S}$ is ambiguous because there are two distinct regimes of interest – one of low curvature and another of high curvature, so this substitution is not considered.

The estimates previously discussed are also valid in special cases of packings of equal area (rather than equal-s) particles. In this scenario Eqs.10 and 11 collapse to:

$$\kappa_{i,j,S} > \kappa_{i,j,C} \Rightarrow \eta_S/\eta_C > 1 \tag{12}$$

$$\kappa_{i,j,C} < \kappa_0 - \kappa_{i,j,S} \wedge \kappa_{i,j,S} > \kappa_0/2 \Rightarrow \eta_S/\eta_C < 1 \tag{13}$$

respectively. Eqs.6, 8 and the consequences of Eqs.10 and 11 are all consistent with the observations outlined in this work. There are certainly significant limitations with this formulation, especially since the inequalities considered in Eqs.10-13 are only valid over certain intervals, heavy assumptions are made about the independence of the bending free energies with respect to the degree of packing and membrane curvatures, and the free energy associated with packing steric pressure was not considered. Nonetheless, this simple thermodynamic approach can be used to partially explain the curvature preferences of the particle species studied here.

4 Conclusion

This study demonstrates that cube-shaped $CsPbBr_3$ embedded in GUV membranes, in contrast to conventional QDs such as CdSe, tend to concentrate greatest in areas of lowest relative curvature. We show that this is due in large part to the geometry differences between $CsPbBr_3$ and CdSe or ATTO-488; cubic structures comparable in scale to the thickness of the lipid bilayer will tend to pack most densely where their aggregate curvature is minimized[33]. Consequently, this system is analogous to curvature-induced protein aggregation, which also have defined curvature preferences based on the interplay between their own geometry and a target surface. Furthermore, the work outlined here provides additional insight into the study of nonspherical nanoparticle-lipid membrane complexes. For instance, while embedded QDs are discussed here, one could consider a related system where curvature-sensitive non-spherical particles could "sense" the curvature of a membrane from the exterior of the vesicle; this system has previously been explored in the context of exterior nanoparticle-mediated membrane poration and deformation[13].

Conflicts of interest

There are no conflicts to declare.

Acknowledgements

This work was supported by the National Science Foundation (Award number NSF PHY-1915017). The authors would also like to thank Lanja Karadaghi at the Department of Chemistry, University of Southern California, for supplying the precursor solutions for the $CsPbBr_3$ quantum dots.

Notes and references

1 H. Mary and G. J. Brouhard, *bioRxiv*, 2019, 1–14.
2 J. Schindelin, I. Arganda-Carreras, E. Frise, V. Kaynig, M. Longair, T. Pietzsch, S. Preibisch, C. Rueden, S. Saalfeld, B. Schmid, J. Y. Tinevez, D. J. White, V. Hartenstein, K. Eliceiri, P. Tomancak and A. Cardona, *Nat. Methods*, 2012, **9**, 676–682.
3 *Created with BioRender.com*.
4 W. F. Zeno, A. S. Thatte, L. Wang, W. T. Snead, E. M. Lafer and J. C. Stachowiak, *J. Am. Chem. Soc.*, 2019, **141**, 10361–10371.
5 O. G. Mouritsen, *Eur. J. Lipid Sci. Technol.*, 2011, **113**, 1174–1187.
6 B. Antonny, *Annual Review of Biochemistry*, 2011, **80**, 101–123.
7 R. Philips, T. Ursell, P. Wiggins and P. Sens, *Nature*, 2009, **459**, 379–385.
8 D. Marsh, *Biochim. Biophys. Acta Biomembr.*, 2008, **1778**, 1545–1575.
9 M. S. Terakawa, Y. Lin, M. Kinoshita, S. Kanemura, D. Itoh, T. Sugiki, M. Okumura, A. Ramamoorthy and Y.-H. Lee, *Biochim. Biophys. Acta Biomembr.*, 2018, **1860**, 1741–1764.
10 D. Parton, J. Klingelhoefer and M. Sansom, *Biophys. J.*, 2011, **101**, 691–699.
11 N. Ramakrishnan, P. Sunil Kumar and J. H. Ipsen, *Biophys. J.*, 2013, **104**, 1018–1028.
12 P. C. Hu, S. Li and N. Malmstadt, *ACS Appl. Mater. Interfaces*, 2011, **3**, 1434–1440.
13 S. Li and N. Malmstadt, *Soft Matter*, 2013, **9**, 4969–4976.

14 X. Michalet, F. F. Pinaud, L. A. Bentolila, J. M. Tsay, S. Doose, J. J. Li, G. Sundaresan, A. M. Wu, S. S. Gambhir and S. Weiss, *Science*, 2005, **307**, 538–544.

15 S. T. Selvan, P. K. Patra, C. Y. Ang and J. Y. Ying, *Angew. Chem.*, 2007, **119**, 2500–2504.

16 J. B. Delehanty, H. Mattoussi and I. L. Medintz, *Anal. Bioanal. Chem.*, 2009, **393**, 1091–1105.

17 M. Wlodek, M. Kolasinska-Sojka, M. Szuwarzynski, S. Kereïche, L. Kovacik, L. Zhou, L. Islas, P. Warszynski and W. H. Briscoe, *Nanoscale*, 2018, **10**, 17965–17974.

18 H. S. Wi, S. J. Kim, K. Lee, S. M. Kim, H. S. Yang and H. K. Pak, *Colloids Surf. B*, 2012, **97**, 37–42.

19 W. Zheng, Y. Liu, A. West, E. E. Schuler, K. Yehl, R. B. Dyer, J. T. Kindt and K. Salaita, *J. Am. Chem. Soc.*, 2014, **136**, 1992–1999.

20 Y. Tang, Z. Li, Z. T. Li, J. S. Li, S. D. Yu and L. S. Rao, *IEEE Trans. Electron Devices*, 2018, **65**, 158–164.

21 C. Tosat-Bitrián, A. Avis-Bodas, G. Porras, D. Borrego-Hernández, A. García-Redondo, A. Martín-Requero and V. Palomo, *Nanomaterials*, 2021, **11**, 1–15.

22 T. Okano, K. Inoue, K. Koseki and H. Suzuki, *ACS Synth. Biol.*, 2018, **7**, 739–747.

23 W. Zong, Q. Li, X. Zhang and X. Han, *Colloids Surf. B*, 2018, **172**, 459–463.

24 L. Wang, L. R. Karadaghi, R. L. Brutchey and N. Malmstadt, *Chem. Commun.*, 2020, **56**, 3745–3748.

25 A. Elbaradei, L. C. Dalle Ore and N. Malmstadt, *J. Vis. Exp.*, 2021, 1–14.

26 J. Sykes, *Tissue Culture*, Academic Press, 1973, pp. 303–308.

27 H. Terasawa, K. Nishimura, H. Suzuki, T. Matsuura and T. Yomo, *Proc. Natl. Acad. Sci. U.S.A.*, 2012, **109**, 5942–5947.

28 S. Mukherjee and F. R. Maxfield, *Annual Review of Cell and Developmental Biology*, 2004, **20**, 839–866.

29 G. van Meer, D. R. Voelker and G. W. Feigenson, *Nature Reviews Molecular Cell Biology*, 2008, **9**, 112–124.

30 S. R. Sternberg, *IEEE Computer*, 1983, **16**, 22–34.

31 I. The MathWorks, *hist3*, `https://www.mathworks.com/help/stats/hist3.html`, Online; accessed 26 Feb 2023.

32 D. M. Lane, D. Scott, M. Hebl, R. Guerra, D. Osherson and H. Zimmer, *Online Statistics: An Interactive Multimedia Course of Study*, Rice University and University of Houston technical report, 2005.

33 S. X. Li, J. Zhao, P. Lu and Y. Xie, *Chinese Science Bulletin*, 2010, **55**, 114–119.

34 J. Tian, Y. Xu, Y. Jiao and S. Torquato, *Sci. Rep.*, 2015, **5**, 1–9.

35 S. I. Galiev and M. S. Lisafina, *Comput. Math. Math. Phys.*, 2013, **53**, 1748–1762.

36 H. S. Wi, K. Lee and H. K. Pak, *J. Condens. Matter Phys.*, 2008, **20**, 494211–494217.

37 S. K. Sung, H. K. Pak, J. H. Kwak, S. W. Lee, Y. H. Kim, B. I. Hur, S. J. Jin and G. R. Kim, *Open J. Biophys.*, 2018, **8**, 163–175.

38 J. A. Peacock, *Mon. Notices Royal Astron. Soc.*, 1983, **202**, 615–627.

39 D. Muir, *kstest_2s_2d(x1,x2,alpha)*, `https://www.mathworks.com/matlabcentral/fileexchange/38617-kstest_2s_2d-x1-x2-alpha`, Online; accessed 19 Feb 2023.

40 W. F. Zeno, A. Rystov, D. Y. Sasaki, S. H. Risbud and M. L. Longo, *Langmuir*, 2016, **32**, 4688–4697.